J. Fluid Mech. (2006), *vol.* 568, *pp.* 89–108.
doi:10.1017/S0022112006002060 Printed in the United Kingdom

The transition from geostrophic to stratified turbulence

By MICHAEL L. WAITE† AND PETER BARTELLO

McGill University, 805 rue Sherbrooke ouest, Montréal, QC H3A 2K6, Canada

(Received 1 April 2005 and in revised form 9 April 2006)

We present numerical simulations of forced rotating stratified turbulence dominated by vortical motion (i.e. with potential vorticity). Strong stratification and various rotation rates are considered, corresponding to a small Froude number and a wide range of Rossby numbers Ro spanning the regimes of stratified turbulence ($Ro = \infty$) to quasi-geostrophic turbulence ($Ro \ll 1$). We examine how the energy spectra and characteristic vertical scale of the turbulence vary with Rossby number between these two regimes. The separate dependence on N/f, where N is the Brunt–Väisälä frequency and f is the Coriolis parameter, is found to be of secondary importance. As the macroscale Ro decreases below 0.4 and the microscale Ro (at our resolution) decreases below 3, the horizontal wavenumber energy spectrum steepens and the flat range in the vertical wavenumber spectrum increases in amplitude and decreases in length. At large Rossby numbers, the vertical scale H is proportional to the stratified turbulence value U/N, where U is the root mean square velocity. At small Ro, H takes the quasi-geostrophic form $(f/N)L$, where L is the horizontal scale of the flow. Implications of these findings for numerical atmosphere and ocean modelling are discussed.

1. Introduction

The dynamics of the atmosphere and the ocean are influenced by stable density stratification and the Earth's rotation, and the importance of these effects varies with scale. At the largest geophysical scales, rotation and stratification are both significant, and the Rossby and Froude numbers

$$Ro = \frac{U}{fL}, \quad Fh = \frac{U}{NL}, \quad Fz = \frac{U}{NH}, \tag{1.1}$$

are small. Quasi-geostrophic (QG) turbulence dominates at these scales. Here U, L and H are characteristic velocity, horizontal and vertical length scales that are diagnosed from the flow (see (3.7) and (3.8)); f is the Coriolis parameter; and N is the Brunt–Väisälä frequency. The influence of rotation and stratification weakens as one moves downscale. According to the classical view, rotation weakens more rapidly than stratification since $N/f \sim O(100)$ over most of the atmosphere and ocean. The atmospheric mesoscale (horizontal scales of kilometres to hundreds of kilometres) and oceanic submesoscale (tens of metres to tens of kilometres)

† Present address: National Center for Atmospheric Research, PO Box 3000, Boulder, CO, 80307-3000, USA. The National Center for Atmospheric Research is sponsored by the National Science Foundation.

are characterized by strong stratification, but only moderate rotation ($Ro \gtrsim 1$; e.g. Emanuel 1986). Stratified turbulence (with $Ro = \infty$) is often studied as a first approximation to this regime. In this work, we examine the influence of rotation on stratified turbulence.

Stably stratified flows can be decomposed into vortical motion and internal inertia–gravity waves using potential vorticity (PV). Vortical motion is defined to account for all the PV, while the inertia–gravity waves have no PV (e.g. Staquet & Riley 1989; this definition can be difficult in practice, and the standard linear approximation to it is employed below). Because we are interested in the transition between geostrophic and stratified turbulence, we limit ourselves in this study to flows dominated by vortical motion rather than internal waves. Vortical motion makes up a significant part of the flow in the atmospheric mesoscale (e.g. Cho *et al.* 1999*b*), but not necessarily in the oceanic submesoscale (e.g. Polzin *et al.* 2003). We further restrict our analysis to homogeneous turbulence, and examine two quantities: the (anisotropic) energy spectrum and the associated vertical length scale. These quantities are increasingly well accounted for in the limiting regimes of QG turbulence and stratified turbulence without rotation. This intermediate regime, however, remains poorly understood.

In the QG case, the classical theory is due to Charney (1971), who argued that QG turbulence is isotropic in the scaled vertical coordinate $(N/f)z$, implying a vertical scale $H \sim (f/N)L$. This scaling has been verified in numerical simulations of QG turbulence, which found $H \approx 0.8(f/N)L$ (Reinaud, Dritschel & Koudella 2003). Charney (1971) gave a phenomenological argument for an isotropic (in scaled coordinates) energy spectrum of the form k^{-3}, which has been observed in the atmosphere (e.g. Nastrom & Gage 1985) and in numerical simulations (McWilliams, Weiss & Yavneh 1994).

In stratified turbulence without rotation, vortical motion is not geostrophic, and the classical QG theory does not apply. The atmospheric mesoscale energy spectrum has the form $k_h^{-5/3}$ (k_h is the horizontal wavenumber; e.g. Nastrom & Gage 1985; Cho *et al.* 1999*a*), and numerical simulations of stratified turbulence have generated consistent results when vigorous small-scale static instability (overturning) is present (e.g. Riley & deBruynKops 2003; Waite & Bartello 2004; Lindborg 2005, 2006). When overturning is suppressed by dissipation, the spectrum appears to steepen to k_h^{-5} (Laval, McWilliams & Dubrulle 2003; Waite & Bartello 2004). The limiting dynamics of strongly stratified vortical motion are decoupled layers of quasi-horizontal flow, which implies a vertical scale collapse as $Fh \to 0$ (Riley, Metcalfe & Weissman 1981; Lilly 1983). Billant & Chomaz (2001) argued that H scales like U/N in stratified turbulence, suggesting that $Fz \equiv 1$ as $Fh \to 0$. This scaling has been observed in recent numerical simulations, which found that the layers of stratified turbulence are coupled by overturning and small-scale turbulence at vertical scales of U/N, where U is the root mean square (r.m.s.) velocity (Waite & Bartello 2004; Lindborg 2006). The vertical wavenumber spectra are correspondingly flat out to $k_z \sim N/U$. In addition, many recent studies of forced stratified turbulence have found a slow systematic transfer of energy into vertically sheared, horizontally uniform velocity (modes with $k_h = 0$, i.e. the shear modes or, when $f \neq 0$, inertial oscillations) (Smith & Waleffe 2002; Laval *et al.* 2003; Waite & Bartello 2004, 2006).

This paper builds on the study of Waite & Bartello (2004) by examining numerically the intermediate regime of strongly stratified rotating turbulence between the non-rotating and QG limits. As the rotation rate is gradually increased from zero, the energy spectra and vertical length scales of stratified turbulence ($k_h^{-5/3}$, k_z^0 for $k_z < N/U$, $H \propto U/N$) must evolve to those of QG turbulence (k^{-3}, $H \propto (f/N)L$). Our aim in

this study is to investigate how this transition occurs. Dimensionally, H depends independently on Ro and N/f, and takes the form

$$H = \frac{U}{N} G(Ro, N/f), \tag{1.2}$$

if dissipation effects can be neglected. Babin, Mahalov & Nicolaenko (1998) have argued that very weak rotation will couple ('glue') the layers of stratified turbulence together such that H takes the QG value $(f/N)L$ even when $Ro \gg 1$. However, $U/N > (f/N)L$ when $Ro > 1$, and so this coupling may be obscured by overturning and small-scale turbulence unless $Ro < 1$. Billant & Chomaz (2001) have accounted for this complication and argue that H transitions from $(f/N)L$ (when $Ro \ll 1$) to U/N (when $Ro \gg 1$) around $Ro \sim 1$. In other words, G is a function of Ro alone and not N/f. Lindborg (2005) finds that the transition from stratified to QG turbulence, defined by the emergence of an inverse cascade, occurs at $Ro \sim 0.1$. To the best of our knowledge, however, a numerical study of the transition of H between these two regimes has not been made.

To investigate these issues, we have performed a set of simulations of forced strongly stratified turbulence over a wide range of rotation rates ($O(0.1) \lesssim Ro \leqslant \infty$), and examined how the energy spectra and length scales vary with Rossby number. In the next section, we present the Boussinesq equations and discuss the normal mode decomposition into vortical and wave parts. Our numerical methodology is described in § 3. In § 4, we present the results of our primary simulations and show how the energy spectra and vertical length scales vary with Ro. In § 5, we discuss the dependence of our results on N/f. Conclusions are given in § 6.

2. Governing equations

Making the Boussinesq approximation, the equations of motion for a rotating stratified fluid are

$$\frac{\partial \boldsymbol{u}}{\partial t} + \boldsymbol{u} \cdot \nabla \boldsymbol{u} + f \hat{\boldsymbol{z}} \times \boldsymbol{u} = -\nabla p + b' \hat{\boldsymbol{z}} + \boldsymbol{F}_u + D_u(\boldsymbol{u}), \tag{2.1a}$$

$$\nabla \cdot \boldsymbol{u} = 0, \tag{2.1b}$$

$$\frac{\partial b'}{\partial t} + \boldsymbol{u} \cdot \nabla b' + N^2 w = F_{b'} + D_{b'}(b'), \tag{2.1c}$$

where $\boldsymbol{u} = u\hat{\boldsymbol{x}} + v\hat{\boldsymbol{y}} + w\hat{\boldsymbol{z}}$ is the velocity, b' is the buoyancy, and p is the dynamic pressure divided by a reference density. $D_q(q)$ and F_q denote the dissipation and forcing of the quantity q, respectively. We limit our study to homogeneous turbulence and therefore take f and N to be constant.

When expressed in terms of the linear normal mode basis, the Fourier-transformed Boussinesq equations take the compact form

$$\frac{\mathrm{d}B_{\boldsymbol{k}}^{(j)}}{\mathrm{d}t} + \mathrm{i}\lambda_{\boldsymbol{k}}^{(j)} B_{\boldsymbol{k}}^{(j)} = \sum_{\boldsymbol{k}=\boldsymbol{p}+\boldsymbol{q}} \Gamma_{\boldsymbol{k}\boldsymbol{p}\boldsymbol{q}}^{jrs} B_{\boldsymbol{p}}^{(r)} B_{\boldsymbol{q}}^{(s)} + \hat{F}_k^{(j)} + \hat{D}_k^{(j)}, \tag{2.2}$$

where j is 0 or $\pm$ (following Bartello 1995; see Appendix A). In (2.2), $B_{\boldsymbol{k}}^{(0)}$, $B_{\boldsymbol{k}}^{(+)}$ and $B_{\boldsymbol{k}}^{(-)}$ are the amplitudes of the three normal modes at wavevector $\boldsymbol{k}$, and the Γ are the interaction coefficients. The normal modes have linear frequencies $\lambda_{\boldsymbol{k}}^{(j)}$ given by

$$\lambda_{\boldsymbol{k}}^{(0)} = 0, \quad \lambda_{\boldsymbol{k}}^{(\pm)} = \left(N^2 k_h^2 + f^2 k_z^2\right)^{1/2} / k, \tag{2.3a, b}$$

where $k_h = (k_x^2 + k_y^2)^{1/2}$ and $k = (k_x^2 + k_y^2 + k_z)^{1/2}$. The zero frequency mode is known as the vortical mode, and it corresponds to horizontal rotational flow which is (when $f \neq 0$) geostrophically balanced. We refer to the two higher-frequency modes as the wave modes because they satisfy the dispersion relation for inertia–gravity waves. Note however, that when $f \neq 0$, we could equally call $B_{\boldsymbol{k}}^{(0)}$ the geostrophic mode and $B_{\boldsymbol{k}}^{(\pm)}$ the ageostrophic modes, with the latter coming from balanced ageostrophic motion in addition to waves. In this work, we use 'vortical' and 'wave' to be consistent with the full range of f considered.

The normal mode decomposition is linear, and therefore provides only a linear approximation to the dynamically significant PV decomposition. The PV for (2.1) is Π/ρ_0, where

$$\Pi = (\boldsymbol{\omega} + f\hat{\boldsymbol{z}}) \cdot (N^2 \hat{\boldsymbol{z}} + \nabla b'), \tag{2.4}$$

and $\boldsymbol{\omega} = \nabla \times \boldsymbol{u}$ is the vorticity. Vortical modes account for only the linear PV

$$\Pi_1 = N^2 \omega_z + f \frac{\partial b'}{\partial z}. \tag{2.5}$$

Π_1 is a good approximation to Π, and hence the normal modes provide a meaningful decomposition for the flow, when $Fz \ll 1$ (see Appendix B). The normal modes lose their physical interpretation in terms of PV when $Fz \gtrsim 1$, i.e. at vertical scales smaller than U/N.

3. Numerical approach

We have integrated (2.1) with a pseudo-spectral model in a domain of size $(2\pi)^3$ with 180 collocation points in each direction. While our choice of a cubic domain prevents us from attaining the high vertical resolution of Lindborg (2005) (where a small aspect ratio domain was employed), it reduces the likelihood of domain-size effects playing a role in the vertical, at least at large and intermediate Rossby numbers. Aliasing errors were eliminated by truncating Fourier modes cylindrically at k_h, $|k_z| = 60$. Leapfrog time stepping was employed (with $\Delta t = 0.0042$), along with a Robert filter (of 0.004) to stabilize the computational mode (Asselin 1972). We excited vertically uniform vortical modes with the forcing function

$$\hat{F}_k^{(0)} = A(\boldsymbol{k}) G_{\boldsymbol{k}}(t), \tag{3.1a}$$

$$\hat{F}_k^{(\pm)} = 0, \tag{3.1b}$$

where $G_{\boldsymbol{k}}(t)$ is a Gaussian random process correlated over $10\Delta t$, and $A(\boldsymbol{k})$ is centred around $k_h = k_f$ with $k_z = 0$ as

$$A(\boldsymbol{k}) = \begin{cases} a(k_f + 1 - k_h)(k_h - k_f + 1), & |k_h - k_f| \leqslant 1, \quad k_z = 0, \\ 0, & \text{otherwise.} \end{cases} \tag{3.2}$$

The $10\Delta t$ correlation time scale prevents the forcing from exciting the leapfrog computational mode. We have checked that the statistics of the resulting flows are qualitatively insensitive to this time scale when the amplitude a is appropriately rescaled.

The forcing (3.2) is meant to represent large-scale geophysical vortices which break down in the atmospheric mesoscale and oceanic submesoscale. The restriction to modes with $k_z = 0$ is a significant idealization of the real atmosphere and ocean, but it has the advantage of not imposing a vertical scale on the flow; rather, H emerges

f	N/f	Ro_ω	Fh_ω	Fz_ω	Ro_u	Fh_u	Fz_u
0	∞	∞	0.19	0.53	∞	0.026	0.056
1/16	128	25.0	0.19	0.52	3.4	0.026	0.056
1/8	64	12.0	0.19	0.52	1.7	0.026	0.055
1/4	32	6.3	0.19	0.52	0.83	0.026	0.054
1/2	16	3.2	0.19	0.51	0.39	0.025	0.051
3/4	32/3	2.2	0.21	0.49	0.25	0.024	0.051
1	8	1.7	0.21	0.47	0.18	0.022	0.048
3/2	16/3	1.2	0.22	0.42	0.12	0.022	0.040
2	4	0.89	0.22	0.37	0.090	0.022	0.033
4	2	0.47	0.23	0.21	0.048	0.024	0.018
8	1	0.24	0.23	0.10	0.024	0.024	0.0091

TABLE 1. The Coriolis parameters f used in our primary simulations ($N = 8$) along with N/f and the microscale (vorticity-based) and macroscale (velocity-based) Rossby and Froude numbers. The Rossby and Froude numbers are from the simulations with large-scale damping, and are averaged over $70 \leqslant t \leqslant 100$.

spontaneously. The forcing wavenumber k_f was set to 5 and the amplitude a was set, somewhat arbitrarily, to 0.049. This number has no geophysical significance, but since it is related to the energy dissipation rate ϵ, it will determine how all other parameters are to be selected. Velocity and buoyancy were dissipated by fourth-order cylindrical hyperviscosity to maximize the inertial range, i.e.

$$D_q(q) = -\nu \left(\nabla_h^8 + \frac{\partial^8}{\partial z^8} \right) q. \tag{3.3}$$

The dissipation coefficient ($\nu = 6.0 \times 10^{-14}$) was chosen to give a dissipation wavenumber $k_d = (\epsilon/\nu^3)^{1/22}$ of approximately 50.

The balance between forcing and dissipation produces statistically stationary fields in stratified turbulence (ignoring the slow growth of the shear modes), and so time averages can be studied in place of ensemble averages. No such balance is obtained in the QG limit, since vortical mode energy is transferred to large scales as well as small. In order to achieve stationarity at all Rossby and Froude numbers, we have modified the dissipation term to damp velocity and temperature at large scales. In Fourier space, (3.3) is replaced with

$$\hat{D}_{\boldsymbol{k}}(q) = -\left(\nu\left(k_h^8 + k_z^8\right) + r(\boldsymbol{k})\right)\hat{q}_{\boldsymbol{k}}, \tag{3.4}$$

where

$$r(\boldsymbol{k}) = \begin{cases} r_0, & 1 \leqslant k_h \leqslant \sqrt{2}, \\ 0, & \text{otherwise}, \end{cases} \tag{3.5}$$

and $r_0 = 0.05$. All vertical wavenumbers are damped equally, so this process does not bias the vertical scale of the turbulence. In the following section, simulations with and without large-scale damping will be discussed.

We have performed our primary simulations at a single stratification over a range of f. $N = 8$ was chosen to yield a small Froude number, while the f values (between 0 and 8; see table 1) were chosen to span a wide range of Rossby numbers. These are not realistic geophysical values for N and f, and must be interpreted through the Rossby and Froude numbers that they, along with the forcing parameters, produce. Note that by varying f at fixed N, we are not allowing the two parameters Ro and

N/f to vary independently. We will explore the separate dependences on these parameters with additional simulations at different N in § 5.

In order to determine the Rossby and Froude numbers of a computed flow, we must measure U, L and H; these measurements can be made in different ways. Perhaps the most straightforward approach is to deduce U/L and U/H directly from the r.m.s. vorticity, which yields vorticity-based Rossby and Froude numbers

$$Ro_\omega = \frac{\sqrt{[\omega_z^2]}}{f}, \quad Fh_\omega = \frac{\sqrt{[\omega_z^2]}}{N}, \quad Fz_\omega = \frac{\sqrt{[\omega_x^2 + \omega_y^2]/2}}{N}. \tag{3.6a–c}$$

We have employed this definition in previous studies (Waite & Bartello 2004, 2006). However, as pointed out by a referee, these numbers favour the smallest scales when the energy spectrum is sufficiently shallow, and are therefore possibly dependent on the Reynolds number. We refer to Ro_ω, Fh_ω and Fz_ω as the microscale Rossby and Froude numbers.

A second approach is to measure U, L and H independently. We take U to be the r.m.s. velocity, i.e.

$$U = \sqrt{[u^2 + v^2 + w^2]}, \tag{3.7}$$

and deduce L and H from the spectra of vortical mode energy (defined below in equation (4.5)) as

$$H = 2\pi \left(\frac{E^{(0)}}{\int k_z^{1/2} E_z^{(0)}(k_z)\, dk_z} \right)^2, \quad L = 2\pi \left(\frac{E^{(0)}}{\int k_h^{1/2} E_h^{(0)}(k_h)\, dk_h} \right)^2. \tag{3.8a, b}$$

This definition of H exploits the fact that the vertical wavenumber spectrum of vortical energy in a stratified fluid is relatively flat at small wavenumbers and falls off at large wavenumbers. The flat range indicates the vertical scales over which the flow is decoupled. The definition of H in (3.8a) is designed to pick out the length scale of this transition in the spectrum, and L is defined consistently. These scales are discussed at length in Waite & Bartello (2004). We refer to Ro_u, Fh_u and Fz_u as the macroscale Rossby and Froude numbers. Note that the macroscale numbers are defined in terms of a single dominant length and velocity scale, while the microscale numbers are essentially integrals over all scales. In what follows, we will use the macroscale Rossby number to distinguish our simulations. However, the microscale Froude numbers should be kept in mind for comparisons with Waite & Bartello (2004).

All simulations were initialized with a small amount of seed energy with an isotropic spectrum of the form

$$E(k) \propto k^4 \exp(-2(k/k_f)^2), \tag{3.9}$$

and random phases. The initial energy was 0.01 equipartitioned between vortical and wave modes. Simulations were then integrated from $t = 0$ to 100. This is an integration length of around 130 buoyancy periods and 20 eddy turnover times, which we define as $\tau = L/U$. Various quantities were averaged over 500 samples from the last 30 % of the integration. Time-averaged Rossby and Froude numbers are given in table 1. The microscale and macroscale values differ by an $O(10)$ factor, even at small Rossby numbers where (as we shall see below) the energy spectra are steep. Some of this discrepancy is probably due to the factor of 2π, which is included in (3.8) but not (3.6).

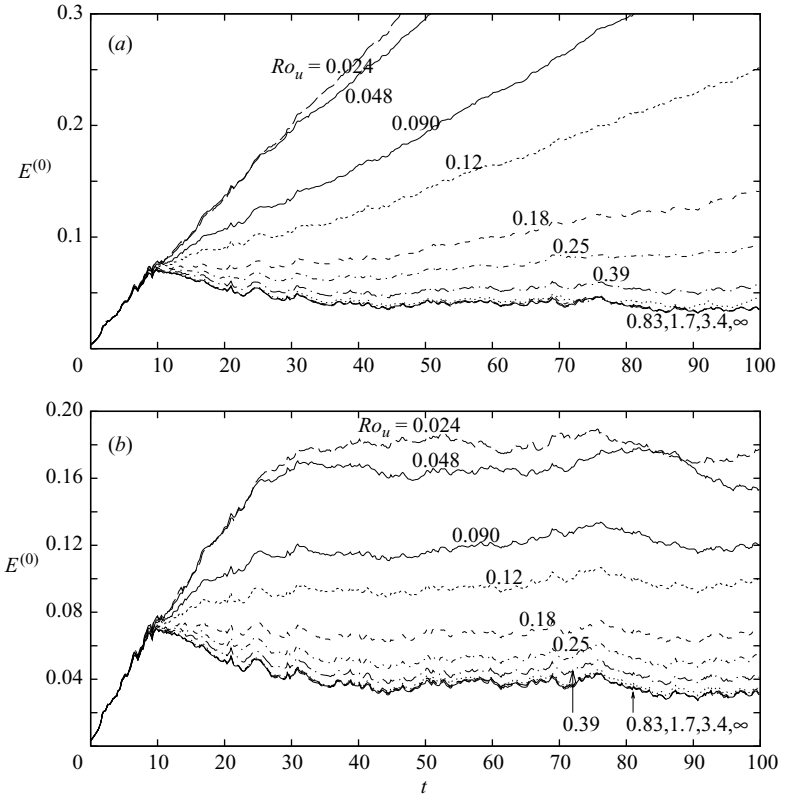

FIGURE 1. Time series of vortical energy for different Ro_u, (*a*) without and (*b*) with large-scale damping. At each time, the energy increases with decreasing Ro_u.

4. Results: fixed N

Time series of vortical energy (with and without large-scale damping) are shown in figure 1. The total energy of the flow has vortical, wave and shear mode contributions, which are given by

$$E^{(0)} = \frac{1}{2}\sum_{k_h\neq 0} \left|B_{\boldsymbol{k}}^{(0)}\right|^2, \tag{4.1a}$$

$$E^{(\pm)} = \frac{1}{2}\sum_{k_h\neq 0} \left|B_{\boldsymbol{k}}^{(+)}\right|^2 + \left|B_{\boldsymbol{k}}^{(-)}\right|^2, \tag{4.1b}$$

$$E^{(S)} = \frac{1}{2}\sum_{k_h=0} |\hat{u}_{\boldsymbol{k}}|^2 + |\hat{v}_{\boldsymbol{k}}|^2 + |\hat{b}'_{\boldsymbol{k}}|^2/N^2. \tag{4.1c}$$

Below we will consider only the kinetic energy in $E^{(S)}$; this is the quantity that was found to grow by Smith & Waleffe (2002) and that corresponds to the energy of inertial oscillations when $f \neq 0$. Vortical energy is injected directly by the forcing, while wave and shear energy are generated via nonlinear interactions. Even without large-scale damping, statistical stationarity is obtained when $Ro_u \geqslant 0.39$. At smaller Rossby numbers, though, vortical energy grows systematically along the entire integration when no large-scale damping is employed. With damping, stationary time series

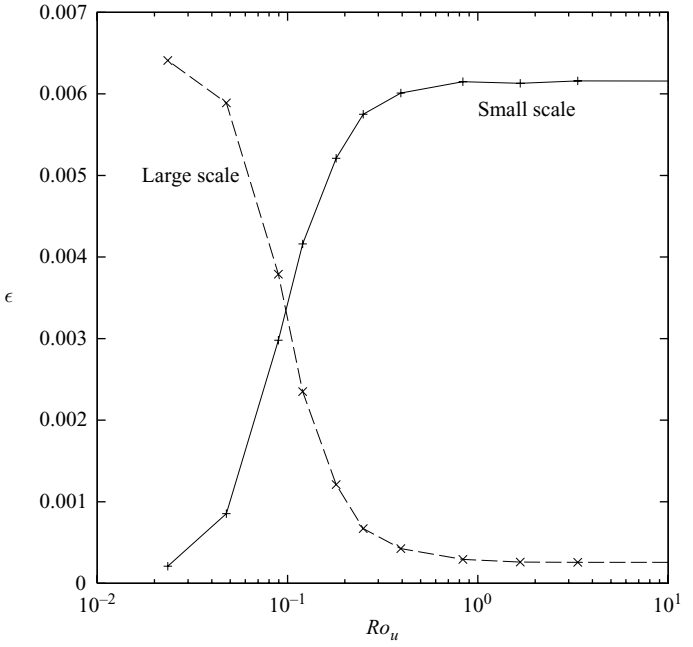

FIGURE 2. The small- and large-scale energy dissipation rates ϵ_s and ϵ_l.

are obtained at all Rossby numbers, although the amount of energy at stationarity increases with decreasing Ro. The strength of the upscale and downscale energy transfer can be quantified by the large-scale and small-scale energy dissipation rates ϵ_l and ϵ_s, which are given by

$$\epsilon_l = 2r_0 \sum_{1 \leqslant k_h \leqslant \sqrt{2}} (|\hat{u}_{\boldsymbol{k}}|^2 + |\hat{v}_{\boldsymbol{k}}|^2 + |\hat{w}_{\boldsymbol{k}}|^2 + |\hat{b}'_{\boldsymbol{k}}|^2/N^2), \tag{4.2a}$$

$$\epsilon_s = 2\nu \sum_{\boldsymbol{k}} \left(k_h^8 + k_z^8\right)(|\hat{u}_{\boldsymbol{k}}|^2 + |\hat{v}_{\boldsymbol{k}}|^2 + |\hat{w}_{\boldsymbol{k}}|^2 + |\hat{b}'_{\boldsymbol{k}}|^2/N^2), \tag{4.2b}$$

and are plotted in figure 2. The transition from a regime dominated by downscale transfer (i.e. stratified turbulence) to one dominated by upscale transfer (i.e. QG turbulence) begins around $Ro_u \approx 0.4$, and the upscale transfer dominates when $Ro_u < 0.1$. These findings agree with those of Lindborg (2005).

A closer look at other quantities, however, reveals that stationarity is in fact not obtained even when rotation is weak. In figure 3, we plot time series of kinetic energy in the shear modes from the undamped simulations (large-scale damping slightly enhances the growth of these modes). The shear mode energy grows in our simulations when $Ro_u \geqslant 0.39$. This growth appears to be inhibited at smaller Rossby numbers, although it may simply be very slow (much longer simulations are required to say for sure). These results suggest that the transfer of energy into the shear modes does not occur, or is greatly inhibited, when the Rossby number is small enough to produce a QG inverse cascade. This transition happens at Ro_u between 0.2 and 0.4, and has $N/f > 10$. QG motion therefore dominates over the shear modes at large scales when the Rossby number is small, even if resonant three-wave interactions are possible, as is the case outside the range $1/2 \leqslant N/f \leqslant 2$. This result can be compared with those of Smith & Waleffe (2002), taking note of the different forcing and time scales.

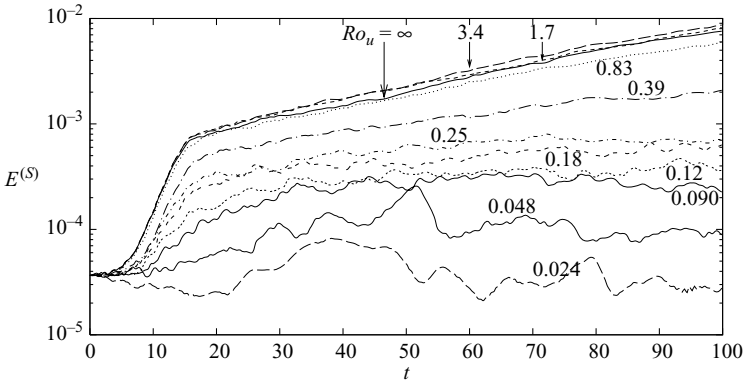

FIGURE 3. Time series of shear mode kinetic energy for different Rossby numbers without large-scale damping. When damping is employed, the growth is slightly enhanced.

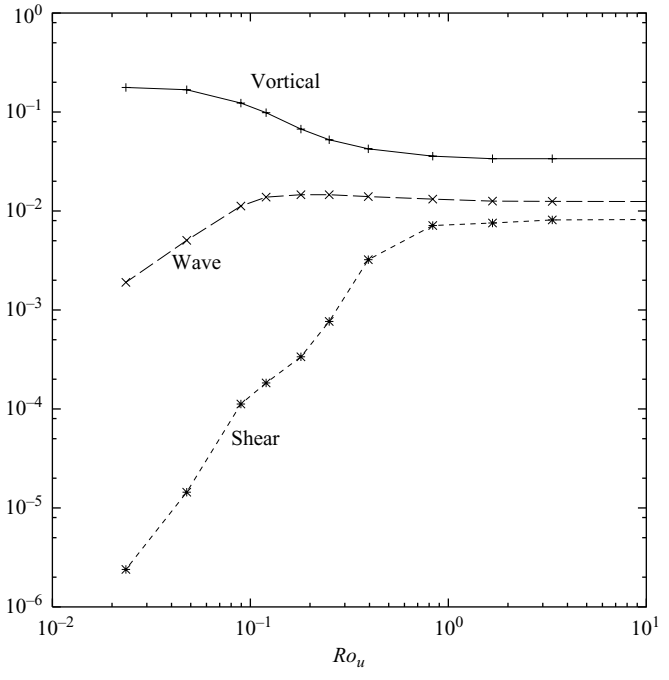

FIGURE 4. The time-averaged vortical, wave and shear mode kinetic energy as defined in § 2 for the simulations with large-scale damping.

The time-averaged vortical, wave and shear mode energies are plotted against Ro_u in figure 4. Vortical energy dominates in all cases, but when $Ro_u > 1$ there is also significant wave and shear energy (this problem was considered in detail in Waite & Bartello 2004). The presence of rotation enhances the amount of vortical energy at statistical stationarity, and the vortical energy increases with decreasing Rossby number below $Ro_u \approx 1$. The dependence on Rossby number appears to weaken as $Ro_u \to 0$ when almost all the injected energy is transferred upscale. The shear mode kinetic energy decreases with decreasing Ro_u when $Ro_u < 1$. The wave energy, by

contrast, is surprisingly insensitive to the Rossby number when $Ro_u > 0.1$. At smaller values, it decreases rapidly as Ro_u decreases, which is consistent with the first-order decoupling discussed by Bartello (1995). Recall that balanced ageostrophic motion makes up an unknown fraction of the wave energy in figure 4.

In order to illustrate the layering of the vortical modes, we have plotted vertical slices of velocity and vorticity for three different Rossby numbers in figure 5 (the normal component is shown in each case). When $Ro_u = \infty$, the flow is dominated by strong vertical layering, although a vertically uniform signal from the forcing is visible. The characteristic stratified turbulence vertical scale U/N is larger than the dissipation scale $l_d = 1/k_d$ and, as a result, small-scale instability and overturning is visible. The layers broaden as the Rossby number decreases. The increase in vertical scale appears more prominently in the velocity field than in the vorticity field, suggesting that the effects of rotation are felt first at large vertical scales as the Rossby number decreases. Indeed, this conclusion is reinforced by figure 6, which plots the number of zero-crossings in vertical profiles of v and ω_y against Ro_u. As Ro_u decreases from ∞, the number of zero-crossings in the velocity field begins to decrease before that of the vorticity field. Since velocity is a larger-scale quantity than vorticity, we conclude that the effects of rotation are felt in the large vertical scales before the small scales.

Horizontal slices of velocity and vorticity (again the normal components, i.e. w and ω_z) are shown in figure 7 for the same Rossby numbers as in figure 5. Without rotation, the vertical vorticity resembles that reported by Waite & Bartello (2004). We see the large-scale vortical structure associated with the forcing, along with patches of small-scale vorticity due to overturning. As the Rossby number decreases, coherent vortices and vortex filaments emerge, but isolated patches of small-scale vorticity remain. The vertical velocity field is correlated with the vorticity field, with strong vertical velocity coinciding with regions of small-scale vertical vorticity, as expected if these regions are characterized by overturning.

There are also correlations between vertical velocity and large-scale vortex structures, especially when $Ro_u = 0.090$. It should be recalled that vertical velocity, although it contributes exclusively to the linear wave modes, is also induced by QG motion. The QG portion of the vertical velocity w_g can be approximated by the omega equation (e.g. Hoskins, Draghici & Davies 1978)

$$\left(N^2\nabla_h^2 + f^2\frac{\partial^2}{\partial z^2}\right) w_g = 2\,\nabla\cdot\boldsymbol{Q} \tag{4.3}$$

where

$$\boldsymbol{Q} = -(\nabla b_g'^{\perp}\cdot\nabla)\,\boldsymbol{u}_g^{\perp}, \tag{4.4}$$

$\boldsymbol{u}_g^{\perp} = (-v_g, u_g)$, u_g and v_g are the components of the geostrophic velocity, b_g' is the corresponding buoyancy from thermal wind balance, and $\nabla b_g'^{\perp} = (-\partial b_g'/\partial y, \partial b_g'/\partial x)$. In figure 8, we plot the resulting vertical velocity for the two finite Rossby numbers in figure 7. The w_g field is noticeably correlated with w at large scales when $Ro_u = 0.090$, but it does not capture the small-scale filamentary structure. The variance of w_g is 5 % of the total w variance when $Ro_u = 0.18$ and 14 % when $Ro_u = 0.090$. This proportion increases to 34 % when $Ro_u = 0.048$ and 60 %

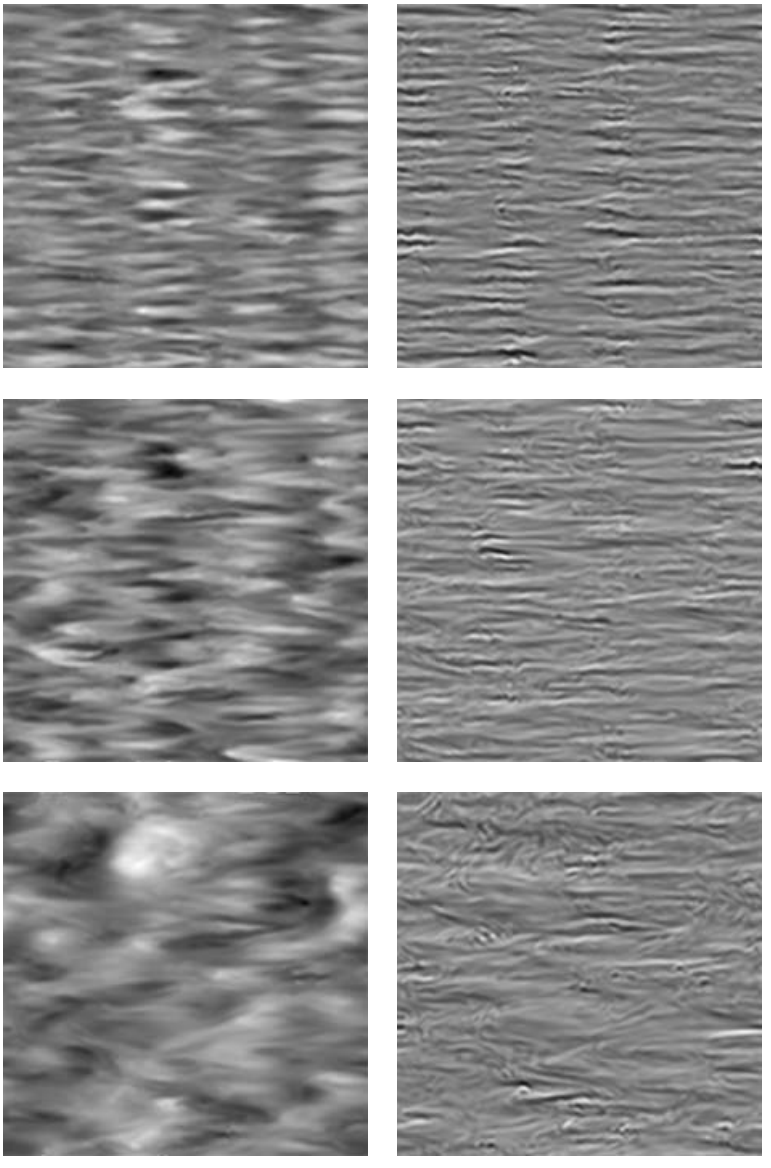

FIGURE 5. Vertical slices (x, z) of the normal velocity v (left) and the normal vorticity ω_y (right) for $Ro_u = \infty$ (top), $Ro_u = 0.18$ (middle) and $Ro = 0.090$ (bottom) at $t = 100$.

when $Ro_u = 0.024$ (not shown). Whether the remainder of w is due to genuine internal gravity waves or to a higher-order balance than (4.3) is unclear from these results.

The horizontal and vertical wavenumber spectra of vortical energy are computed by binning at integer wavenumbers as

$$E_h^{(0)}(k_{h_i}) = \frac{1}{2} \sum_{\boldsymbol{k}' \in I_h(k_{h_i})} \left| B_{\boldsymbol{k}'}^{(0)} \right|^2, \quad E_z^{(0)}(k_{z_i}) = \frac{1}{2} \sum_{\boldsymbol{k}' \in I_z(k_{z_i})} \left| B_{\boldsymbol{k}'}^{(0)} \right|^2, \qquad (4.5a, b)$$

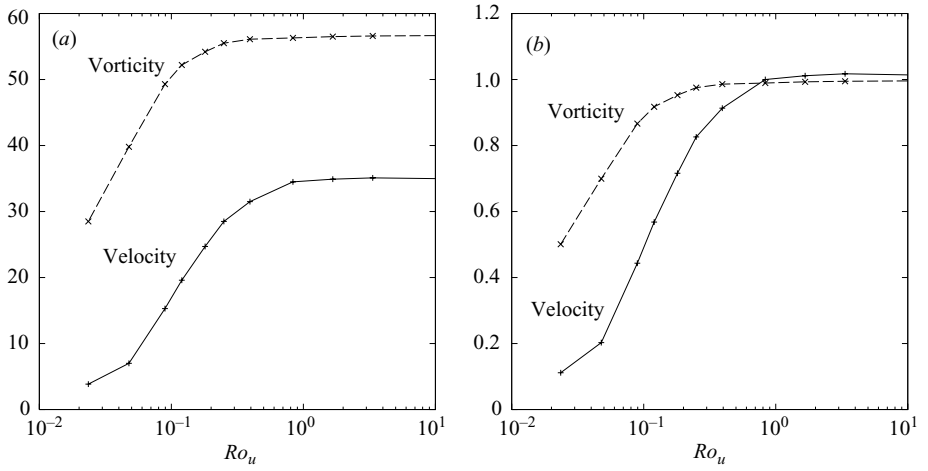

FIGURE 6. (*a*) The number of zero crossings in vertical profiles of v and ω_y averaged over x and y at $t = 100$, and (*b*) the same quantity normalized by its value at $Ro = \infty$.

where

$$I_h(k_{h_i}) = \{\boldsymbol{k}' \,|\, k_{h_i} - 1/2 \leqslant |k'_h| < k_{h_i} + 1/2\}, \tag{4.6a}$$

$$I_z(k_{z_i}) = \{\boldsymbol{k}' \,|\, k_{z_i} - 1/2 \leqslant k'_z < k_{z_i} + 1/2, \quad k_h \neq 0\}. \tag{4.6b}$$

Time-averaged spectra (with large-scale damping) are plotted in figure 9. When $Ro_u \geqslant 0.83$, they are not significantly affected by rotation. The horizontal wavenumber spectra are peaked at $k_h = k_f$, and their spectral slopes (measured by a least-squares power-law fit over $10 \leqslant k_h \leqslant 30$) are around -2.7. This value is between $-5/3$ (thought to result in stratified turbulence when vigorous overturning is present) and -5 (obtained when no overturning is present; see Waite & Bartello 2004). Increasing the vertical resolution leads to a shallowing of the spectrum towards $-5/3$ (not shown). By contrast, the vertical wavenumber spectra at these Rossby numbers are flat along $1 \leqslant k_z \leqslant 20$, which suggests that vertical layers are decoupled across these scales. The spectra steepen somewhat along $20 \leqslant k_z \leqslant 40$, and then fall off rapidly owing to dissipation.

When $Ro_u \leqslant 0.39$, the vertical and horizontal wavenumber spectra are very sensitive to the presence of rotation. The transfer of vortical energy to small horizontal scales is inhibited as the Rossby number decreases; the spectra steepen at large k_h while energy accumulates at small k_h. The vertical wavenumber spectra evolve in a similarly systematic way: the flat range increases in amplitude and decreases in length as Ro_u goes from 0.39 to 0.090. The increased amplitude of the flat range down to $|k_z| = 1$ indicates that rotation is indeed modifying the large vertical scales. When $Ro_u = 0.18$, the flat range is reduced to around $1 \leqslant k_z \leqslant 10$, and when $Ro_u = 0.090$ it is, at most, only a couple of points long. No flat range remains at smaller Rossby numbers, where both the k_h and k_z spectral slopes are steeper than -3, as expected for QG turbulence at this resolution.

The above results appear to confirm the notion that rotation couples the layers of stratified turbulence together; but are the layers 'glued' together by rotation, or are they broadened by an increased value of U/N? In figure 10, we plot H along

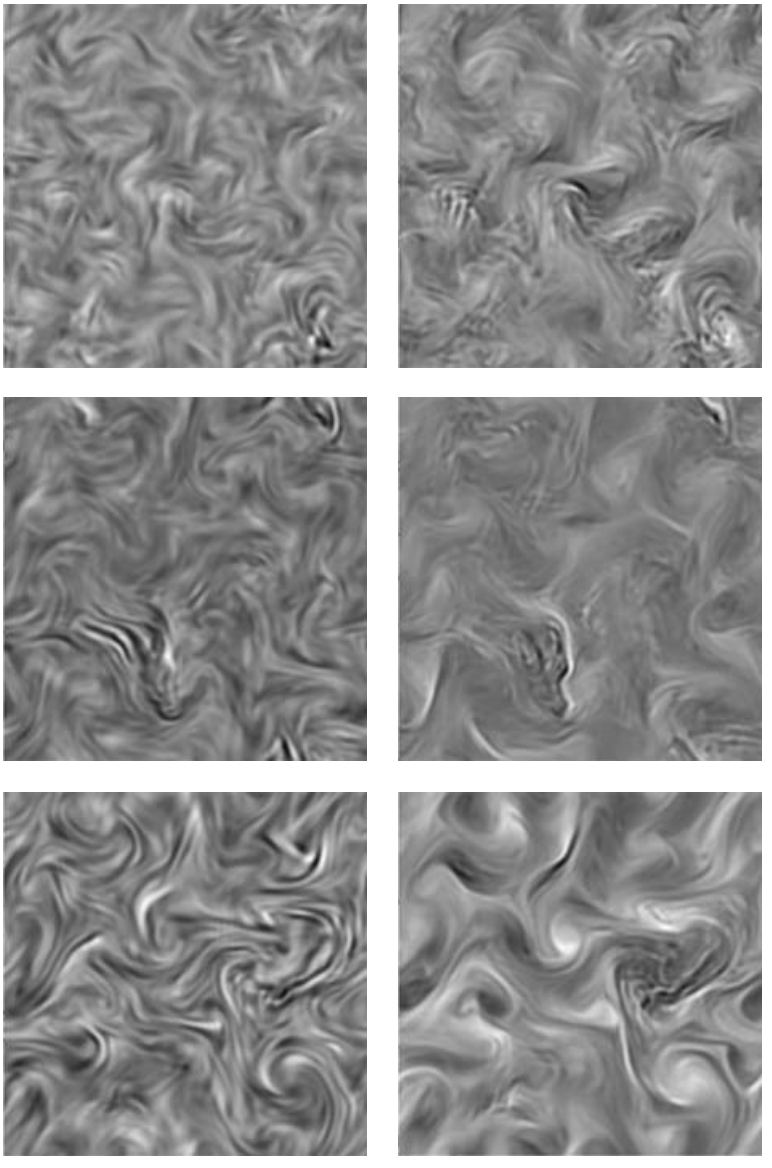

FIGURE 7. Horizontal slices (x, y) of the normal velocity w (left) and the normal vorticity ω_z (right) for $Ro_u = \infty$ (top), $Ro_u = 0.18$ (middle) and $Ro = 0.090$ (bottom) at $t = 100$.

with U/N and $(f/N)L$ against Rossby number. H increases with decreasing Ro_u as expected from figures 5 and 9, but so does (to a lesser degree) U/N. The increase in the layer thickness appears to be accounted for by an enhanced U/N as Ro_u decreases to 0.25, but at smaller Ro_u, H and U/N diverge rapidly. We note that when $Ro_u > 0.25$, U/N appears to under-predict H by a factor of 10 using the precise definitions that we have adopted; nevertheless, in the next section we show that the scaling $H \propto U/N$ holds. When $Ro_u \leqslant 0.18$, H is proportional to the QG scale $(f/N)L$.

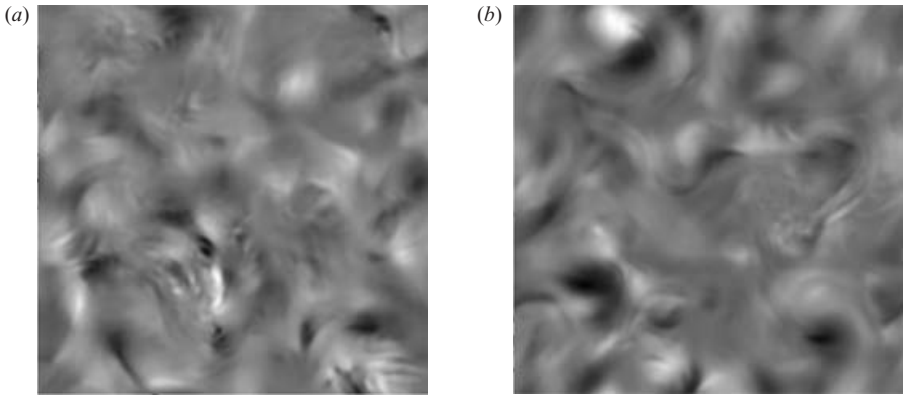

FIGURE 8. Horizontal slices (x, y) of QG vertical velocity w_g given by (4.3) for (a) $Ro_u = 0.18$ and (b) 0.090 at $t = 100$.

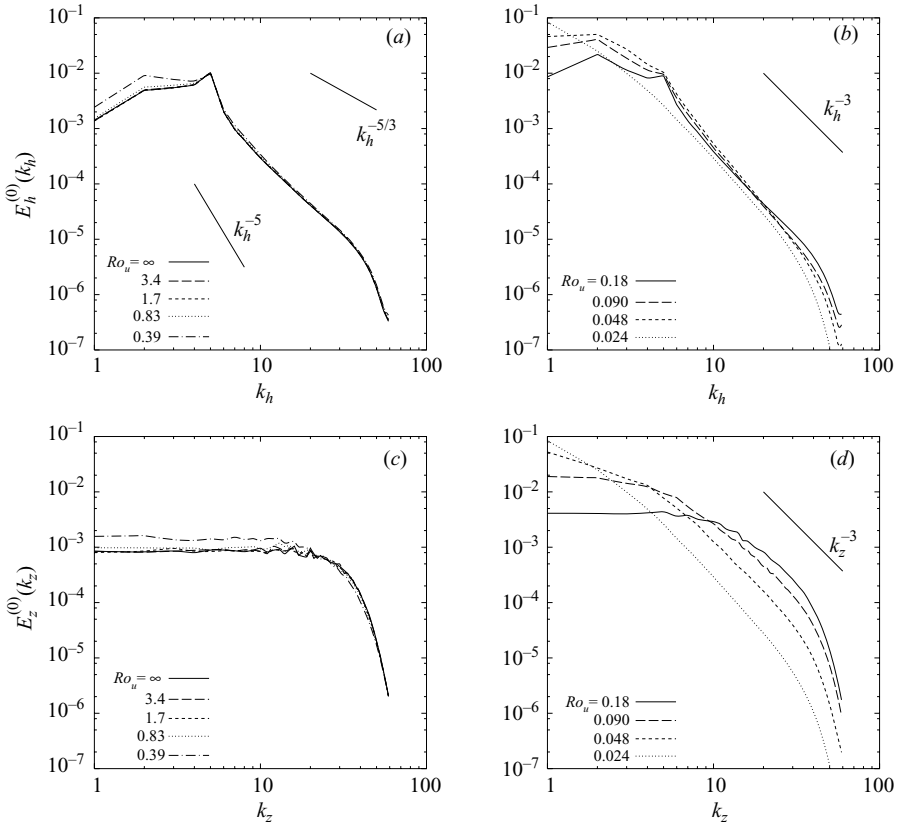

FIGURE 9. Horizontal wavenumber spectra (a, b) and vertical wavenumber spectra (c, d) of vortical energy for $0.39 \leqslant Ro_u \leqslant \infty$ (a, c) and $0.024 \leqslant Ro_u \leqslant 0.18$ (b, d).

5. Dependence on N/f

The simulations described above cover a wide range of Rossby numbers at a fixed stratification of $N = 8$. The characteristic vertical scale H may depend independently on Ro and N/f, and a set of simulations at a fixed N is not able to distinguish

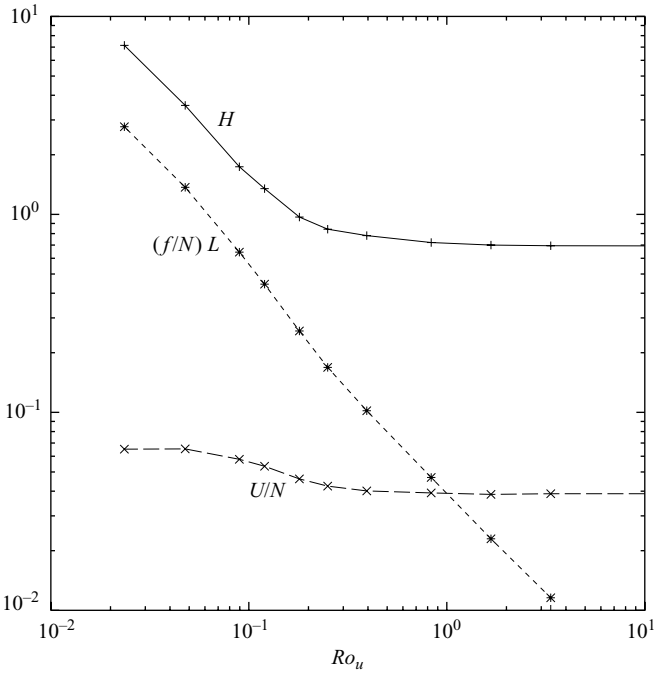

FIGURE 10. Vertical scales as a function of Ro: the measured vertical scale H, the QG scale $(f/N)L$, and U/N.

between these dependencies. Billant & Chomaz (2001) have argued that the N/f dependence is not significant, and that $(N/U)H$ is therefore a universal function of Ro as long as dissipation effects are unimportant. Additional simulations at different N are required to determine whether this is indeed the case.

We have performed two further sets of simulations, one at $N = 4$ and the other at $N = 16$, with ten f values between 0 and 8 and large-scale damping. We followed the same methodology and employed the same forcing and dissipation parameters as described above. The time-averaged vortical, wave and shear kinetic energy are plotted against Ro_u for all three sets of simulations in figure 11. The vortical energy curves collapse for $Ro_u < 0.2$, suggesting that dependence on N/f is weak in this regime. At larger Rossby numbers, the vortical energy is insensitive to rotation but dependent on stratification, as expected from Waite & Bartello (2004). The shear energy behaves similarly. The wave energy, by contrast, does not collapse, and appears to depend independently on both Ro_u and N/f.

In figure 12, we plot $(N/U)H$ as a function of Ro_u for each set of simulations. Our data collapses reasonably well to a single curve which goes to the QG limit ($(N/U)H \propto 1/Ro_u$) when $Ro_u \ll 1$ and the stratified turbulence limit ($(N/U)H \approx 20$) when $Ro_u \gg 1$. The transition between these two regimes occurs around $Ro_u \approx 0.2$. There are, however, some exceptions to this universal scaling. At the lowest Rossby number for $N = 4$, ($Ro_u = 0.025$), $(N/U)H$ is much larger than the corresponding values at $N = 8$ and 16. Energy in this case is unable to escape from the forced two-dimensional modes, and so H, as defined in (3.8*a*), is greatly enhanced. Unlike the others, this simulation has stronger rotation than stratification ($N < f$).

The collapse of the curves also fails at large Rossby numbers. This regime was investigated in detail by Waite & Bartello (2004), who found that H scales like U/N

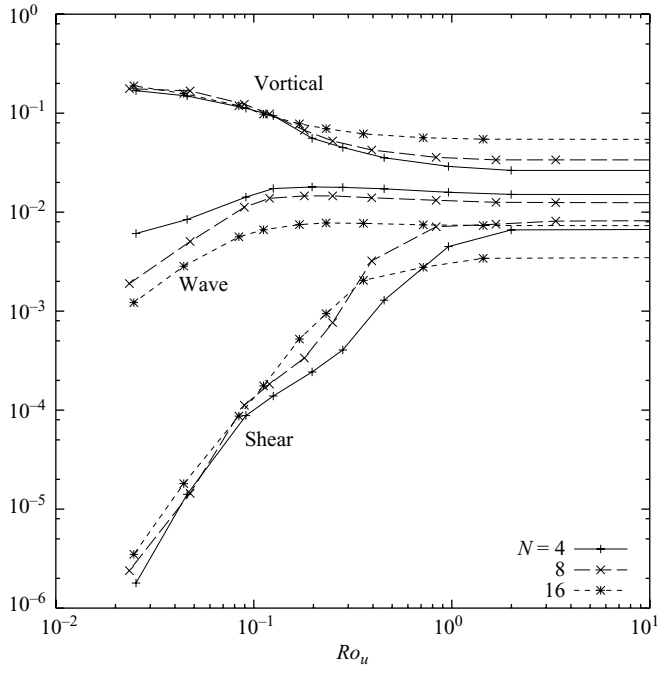

FIGURE 11. The time-averaged vortical, wave and shear mode kinetic energy as defined in § 2 for the sets of simulations with $N = 4$, $N = 8$ (as in figure 4) and $N = 16$.

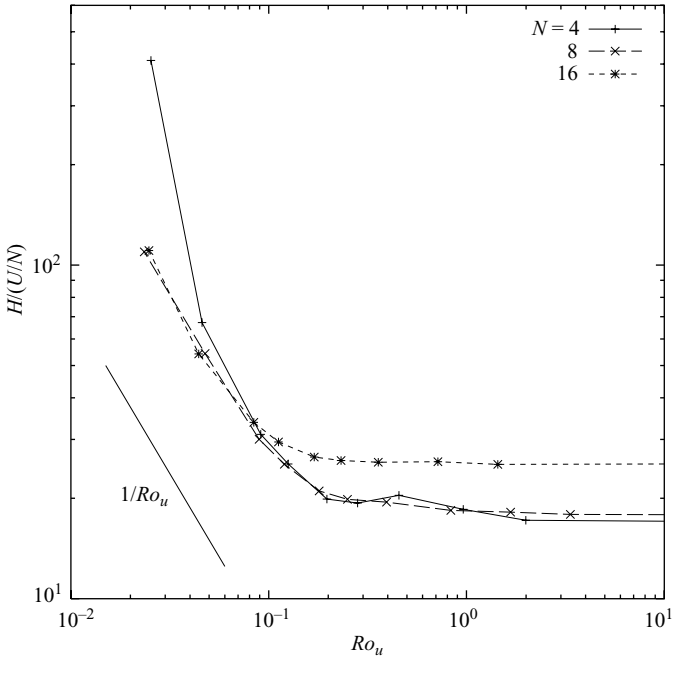

FIGURE 12. The normalized vertical scale $(N/U)H$ for the three sets of simulations $N = 4$, 8 and 16.

as long as U/N is sufficiently larger than the dissipation scale l_d. Viscous effects are important when this condition is not satisfied. Note that Waite & Bartello (2006) found that it is not necessary to have the Ozmidov scale larger than l_d; it is smaller than l_d in all of our cases. In the simulations presented here, only those with $N=4$ and $N=8$ have $U/N > l_d$. When $N=16$, U/N and l_d are not significantly different from one another, and H is set by viscosity as a result. Even in this case, however, the collapse of $(N/U)H$ is excellent as Ro_u decreases below $O(0.1)$ and H increases above the dissipation scale and U/N.

6. Conclusions

We have presented a set of strongly stratified turbulence simulations with two-dimensional vortical mode forcing over a wide range of Rossby numbers. At large Ro, the characteristic vertical scale of the turbulence is $H \propto U/N$, there is no inverse cascade of energy, the energy spectra are insensitive to rotation, and the shear modes grow slowly. At smaller Ro, the effects of rotation are apparent. As the macroscale (velocity-based) Rossby number Ro_u decreases below 0.4 and the microscale (vorticity-based) Rossby number Ro_ω decreases below 3 (at the resolution considered here), some of the injected energy begins to go upscale and the transfer of energy into the shear modes stops (or is greatly inhibited). The energy spectra vary with Ro in this regime: as Ro decreases, the flat range of the k_z spectrum increases in amplitude and decreases in length, while the k_h spectrum steepens beyond a spectral slope of -3. By decreasing Ro with fixed resolution, we are essentially moving upscale through the observed atmospheric k_h spectrum, from the mesoscale towards the QG scales. The vertical scale of the turbulence departs from U/N and, when $Ro_u < 0.2$ ($Ro_\omega < 2$), is proportional to $(f/N)L$.

These observations lead us to conclude that the transition from stratified to quasi-geostrophic turbulence, manifested by the emergence of an inverse cascade, the steepening of the k_h spectrum, and the increase of the vertical scale above U/N, occurs around $Ro_u = 0.4$ and $Ro_\omega = 3$. This conclusion agrees with that of Lindborg (2005), who found an inverse cascade when $Ro_\epsilon = \epsilon^{1/3}/(L^{2/3}f)$ was below 0.1. Using Lindborg's (2005) Rossby number, our transition occurs at $Ro_\epsilon = 0.2$.

Our results indicate that the prediction of Babin *et al.* (1998) that the characteristic vertical scale of rotating stratified turbulence is given by the QG scale $(f/N)L$ does not hold when $Ro \gtrsim 1$, since for these weak rotation rates, the vertical scale is given by the stratified turbulence value U/N. $(N/U)H$ appears to collapse to a universal function of Rossby number as predicted by Billant & Chomaz (2001), as long as U/N is greater than the dissipation scale and $N > f$. Under these conditions, the characteristic vertical scale has no separate dependence on N/f. The velocity and vorticity fields indicate that decreasing the Rossby number affects the large vertical scales before the small scales, in opposition to the analysis of Babin *et al.* (1998). As Ro decreases, we see k_z spectra modified from $k_z \geqslant 1$ and velocity layers growing more dramatically than vorticity layers, underlying the influence of rotation on large vertical scales.

As we move downscale from the large QG scales of the atmosphere and ocean, our simulations suggest that the characteristic vertical scale decreases as $(f/N)L$ until it reaches U/N at $Ro \sim O(1)$, below which it is independent of Rossby number and, as a result, horizontal scale. This conclusion has implications for the choice of the vertical grid spacing Δz in large-scale atmosphere and ocean models as Δx decreases and extends into the atmospheric mesoscale and oceanic submesoscale. At coarse

resolutions, $\Delta z = (f/N)\Delta x$ may be an appropriate choice, but at higher resolutions, Δz is constrained instead by the need to resolve overturning, which sets in at $H \sim U/N$ ($O(1)$ km in the atmosphere and $O(10)$ m in the ocean). Δz need not be as small as $(f/N)\Delta x$ as long as it is sufficiently smaller than U/N. These conclusions are based on our simulations of turbulence dominated by vortical motion. In the future, the influence of rotation on breaking internal waves, which make up an important part of the dynamics of the atmospheric mesoscale and oceanic submesoscale, should also be considered.

This paper benefited greatly from the suggestions of Erik Lindborg and two anonymous reviewers. Financial support from the Natural Sciences and Engineering Research Council of Canada is gratefully acknowledged, as are the computer resources generously provided by the Consortium Laval–UQAM–McGill et l'Est du Québec.

Appendix A. Normal modes

We briefly state the linear normal modes of the Boussinesq equations (2.1) (see Bartello 1995 for details). The Fourier-transformed equations can be written in terms of the three independent variables

$$\zeta_{\boldsymbol{k}} = \mathrm{i}(k_x \hat{v}_{\boldsymbol{k}} - k_y \hat{u}_{\boldsymbol{k}}), \quad D_{\boldsymbol{k}} = \mathrm{i}\frac{k}{k_z}(k_x \hat{u}_{\boldsymbol{k}} + k_y \hat{v}_{\boldsymbol{k}}), \quad T_{\boldsymbol{k}} = \frac{k_h}{N}\hat{b}'_{\boldsymbol{k}}, \tag{A 1}$$

when $k_h \neq 0$ and $k_z \neq 0$. Expressed in this basis, the linear Boussinesq equations without forcing or dissipation take the Hermitian form

$$\frac{\partial}{\partial t}\boldsymbol{W}_{\boldsymbol{k}} = \mathrm{i}L_{\boldsymbol{k}}\boldsymbol{W}_{\boldsymbol{k}}, \tag{A 2}$$

where

$$\boldsymbol{W}_{\boldsymbol{k}} = \begin{pmatrix} \zeta_{\boldsymbol{k}} \\ D_{\boldsymbol{k}} \\ T_{\boldsymbol{k}} \end{pmatrix}, \quad L_{\boldsymbol{k}} = \begin{pmatrix} 0 & \mathrm{i}fk_z/k & 0 \\ -\mathrm{i}fk_z/k & 0 & -Nk_h/k \\ 0 & -Nk_h/k & 0 \end{pmatrix}. \tag{A 3}$$

$\boldsymbol{W}_{\boldsymbol{k}}$ can be expanded in an orthonormal basis given by the eigenvectors of $L_{\boldsymbol{k}}$ as

$$\boldsymbol{W}_{\boldsymbol{k}} = \sum_j A^{(j)}_{\boldsymbol{k}} \boldsymbol{X}^{(j)}_{\boldsymbol{k}}, \tag{A 4}$$

where j is summed over 0, + and −. The eigenvectors are

$$\boldsymbol{X}^{(0)}_{\boldsymbol{k}} = \frac{1}{\sigma_{\boldsymbol{k}} k}\begin{pmatrix} Nk_h \\ 0 \\ -\mathrm{i}fk_z \end{pmatrix}, \quad \boldsymbol{X}^{(\pm)}_{\boldsymbol{k}} = \frac{1}{\sqrt{2}\sigma_{\boldsymbol{k}} k}\begin{pmatrix} \pm\mathrm{i}fk_z \\ \sigma_{\boldsymbol{k}} k \\ \mp Nk_h \end{pmatrix}, \tag{A 5}$$

where

$$\sigma^2_{\boldsymbol{k}} = \frac{N^2 k_h^2 + f^2 k_z^2}{k^2}. \tag{A 6}$$

The amplitudes are expressed in the variables (A 1) as

$$A^{(0)}_{\boldsymbol{k}} = \frac{Nk_h\zeta_{\boldsymbol{k}} + \mathrm{i}fk_z T_{\boldsymbol{k}}}{\sigma_{\boldsymbol{k}} k}, \quad A^{(\pm)}_{\boldsymbol{k}} = \frac{\sigma_{\boldsymbol{k}} k D_{\boldsymbol{k}} \mp \mathrm{i}fk_z\zeta_{\boldsymbol{k}} \mp Nk_h T_{\boldsymbol{k}}}{\sqrt{2}\sigma_{\boldsymbol{k}} k}. \tag{A 7}$$

$A^{(0)}_{\boldsymbol{k}}$ and $A^{(\pm)}_{\boldsymbol{k}}$ are the vortical and wave modes (or, when $f \neq 0$, the geostrophic and ageostrophic modes). Both vertical vorticity and (when $f \neq 0$) vertical buoyancy shear

contribute to the vortical mode. The wave modes account for all of the horizontal divergence as well as (when $f \neq 0$) the inertia-wave component of the vertical vorticity.

In this paper, we employ the normalized normal mode amplitudes $B_{\boldsymbol{k}}^{(j)} = A_{\boldsymbol{k}}^{(j)}/k_h$, since they have the units of velocity. The definition of the $B_{\boldsymbol{k}}^{(j)}$ terms can be expanded to all $\boldsymbol{k}$ by setting

$$B_{\boldsymbol{k}}^{(0)} = \zeta_{\boldsymbol{k}}, \quad B_{\boldsymbol{k}}^{(\pm)} = \hat{w}_{\boldsymbol{k}} \mp \frac{\mathrm{i}\hat{b}'_{\boldsymbol{k}}}{N}, \tag{A 8}$$

when $k_z = 0$, and

$$B_{\boldsymbol{k}}^{(0)} = \frac{\hat{b}'_{\boldsymbol{k}}}{N}, \quad B_{\boldsymbol{k}}^{(\pm)} = \hat{u}_{\boldsymbol{k}} \mp \mathrm{i}\hat{v}_{\boldsymbol{k}}, \tag{A 9}$$

when $k_h = 0$. They are zero when both k_h, $k_z = 0$.

Appendix B. Potential vorticity

The potential vorticity of the Boussinesq equations (2.1) is Π/ρ_0, where Π, given in (2.4), can be expanded to

$$\Pi = \Pi_0 + \Pi_{1b} + \Pi_{1\zeta} + \Pi_2, \tag{B 1}$$

where

$$\Pi_0 = fN^2, \quad \Pi_{1b} = f\frac{\partial b'}{\partial z}, \quad \Pi_{1\zeta} = N^2\omega_z, \quad \Pi_2 = \boldsymbol{\omega}\cdot\nabla b'. \tag{B 2}$$

The subscripts 0, 1 and 2 refer to the order in the variables $\boldsymbol{\omega}$ and b'. Vortical modes contain all the linear PV (Bartello 1995). Our aim is to show that $\Pi_2/(\Pi_{1b}+\Pi_{1\zeta}) \to 0$, i.e. that the linear PV is a good approximation to the full PV, when $Fz \to 0$.

We proceed by performing a straightforward scale analysis of the terms in (B 2). Define scales u, $v \sim U$, $w \sim W$, $b' \sim B$, x, $y \sim L$ and $z \sim H$. Then $\Pi_{1b} \sim fB/H$, $\Pi_{1\zeta} \sim N^2U/L$ and

$$\Pi_2 \sim \max\left(\frac{UB}{LH}, \frac{WB}{L^2}\right) \lesssim \frac{UB}{LH}, \tag{B 3}$$

if we assume that $H \lesssim L$ and $W/H \lesssim U/L$, which is reasonable for rotating stratified turbulence. Balancing the pressure term with the nonlinear term in the u and v components of (2.1) and assuming hydrostatic balance in the w component, the buoyancy term can be shown to scale as $B = U^2/H$, implying

$$\Pi_{1b} \sim f\frac{U^2}{H^2}, \quad \Pi_{1\zeta} \sim N^2\frac{U}{L}, \quad \Pi_2 \lesssim \frac{U^3}{LH^2}. \tag{B 4}$$

The ratio $\Pi_2/(\Pi_{1b} + \Pi_{1\zeta})$ then scales as

$$\frac{\Pi_2}{\Pi_{1b} + \Pi_{1\zeta}} \lesssim \frac{Fz^2}{1 + Fz^2/Ro} \tag{B 5}$$

$$\leqslant Fz^2. \tag{B 6}$$

The linear term therefore dominates the quadratic term when $Fz \ll 1$.

REFERENCES

Asselin, R. 1972 Frequency filter for time integrations. *Mon. Wea. Rev.* **100**, 487–490.

Babin, A., Mahalov, A. & Nicolaenko, B. 1998 On nonlinear baroclinic waves and adjustment of pancake dynamics. *Theor. Comput. Fluid Dyn.* **11**, 215–235.

Bartello, P. 1995 Geostrophic adjustment and inverse cascades in rotating stratified turbulence. *J. Atmos. Sci.* **52**, 4410–4428.

Billant, P. & Chomaz, J.-M. 2001 Self-similarity of strongly stratified inviscid flows. *Phys. Fluids* **13**, 1645–1651.

Charney, J. G. 1971 Geostrophic turbulence. *J. Atmos. Sci.* **28**, 1087–1095.

Cho, J. Y. N., Zhu, Y., Newell, R. E., Anderson, B. E., Barrick, J. D., Gregory, G. L., Sachse, G. W., Carroll, M. A. & Albercook, G. M. 1999*a* Horizontal wavenumber spectra of winds, temperature, and trace gases during the Pacific Exploratory Missions: 1. Climatology. *J. Geophys. Res.* **104**, 5697–5716.

Cho, J. Y. N., Newell, R. E. & Barrick, J. D. 1999*b* Horizontal wavenumber spectra of winds, temperature, and trace gases during the Pacific Exploratory Missions: 2. Gravity waves, quasi-two-dimensional turbulence, and vortical modes. *J. Geophys. Res.* **104**, 16 297–16 308.

Emanuel, K. A. 1986 Overview and definition of mesoscale meteorology. In *Mesoscale Meteorology and Forecasting* (ed. P. S. Ray), pp. 1–17.

Hoskins, B. J., Draghici, I. & Davies, H. C. 1978 A new look at the ω-equation. *Q. J. R. Met. Soc.* **104**, 31–38.

Laval, J.-P., McWilliams, J. C. & Dubrulle, B. 2003 Forced stratified turbulence: successive transitions with Reynolds number. *Phys. Rev.* E **68**, 036308.

Lilly, D. K. 1983 Stratified turbulence and the mesoscale variability of the atmosphere. *J. Atmos. Sci.* **40**, 749–761.

Lindborg, E. 2005 The effect of rotation on the mesoscale energy cascade in the free atmosphere. *Geophys. Res. Lett.* **32**, L010809.

Lindborg, E. 2006 The energy cascade in a strongly stratified fluid. *J. Fluid Mech.* **550**, 207–242.

McWilliams, J. C., Weiss, J. B. & Yavneh, I. 1994 Anisotropy and coherent vortex structures in planetary turbulence. *Science* **264**, 410–413.

Nastrom, G. D. & Gage, K. S. 1985 A climatology of atmospheric wavenumber spectra observed by commercial aircraft. *J. Atmos. Sci.* **42**, 950–960.

Polzin, K. L., Kunze, E., Toole, J. M. & Schmitt, R. W. 2003 The partition of finescale energy into internal waves and subinertial motions. *J. Phys. Oceanogr.* **33**, 234–248.

Reinaud, J. N., Dritschel, D. G. & Koudella, C. K. 2003 The shape of vortices in quasi-geostrophic turbulence. *J. Fluid Mech.* **474**, 175–192.

Riley, J. J. & deBruynKops, S. M. 2003 Dynamics of turbulence strongly influenced by buoyancy. *Phys. Fluids* **15**, 2047–2059.

Riley, J. J., Metcalfe, R. W. & Weissman, M. A. 1981 Direct numerical simulations of homogeneous turbulence in density-stratified fluids. In *Nonlinear Properties of Internal Waves* (ed. B. J. West), pp. 79–112.

Smith, L. M. & Waleffe, F. 2002 Generation of slow large scales in forced rotating stratified turbulence. *J. Fluid Mech.* **451**, 145–168.

Staquet, C. & Riley, J. J. 1989 On the velocity field associated with potential vorticity. *Dyn. Atmos. Oceans* **14**, 93–123.

Waite, M. L. & Bartello, P. 2004 Stratified turbulence dominated by vortical motion. *J. Fluid Mech.* **517**, 281–308.

Waite, M. L. & Bartello, P. 2006 Stratified turbulence generated by internal gravity waves. *J. Fluid Mech.* **546**, 313–339.